ESTIMATING A HIGH-RESOLUTION LUNAR GRAVITY FIELD AND TIME-VARYING CORE SIGNATURE

Ryan S. Park[*]**, Sami W. Asmar**[†]**, Eugene G. Fahnestock**[‡]**, Alex S. Konopliv**[§]**, Wenwen Lu**[¶]**, and Mike M. Watkins**[∥]

This paper presents the expected results of estimating a high-resolution lunar gravity field and time-varying tide and lunar core signatures using the measurements from the Gravity Recovery And Interior Laboratory (GRAIL) mission. An overall GRAIL mission capability is presented based on detailed error analysis of spacecraft dynamics and kinematics models, realistic DSN and inter-spacecraft tracking measurement uncertainties, and length of the data arcs. The largest source of dynamics un-modeled error comes from the spacecraft thermal radiation force, and in order to characterize its error contribution, an *a priori* error constraint model is derived based on orbit geometry and expected force magnitude. The result shows that estimating a lunar gravity field is robust against both dynamics and kinematics errors and a nominal field of degree 300 or better can be determined assuming a $2.5{\times}10^{-4}/n^2$ power law. The resolution of the gravity field is most sensitive to the inter-spacecraft Ka-band tracking accuracy. The core signature, however, is more sensitive to dynamic modeling errors and satisfying the latter science requirements depends on how accurately the spacecraft dynamics can be modeled.

INTRODUCTION

The Gravity Recovery And Interior Laboratory (GRAIL) mission is a part of NASA's Discovery Program. The GRAIL mission is composed of two probes and is scheduled for launch in September 2011 on a Delta-II heavy launch vehicle. The mission is in many ways similar to the Gravity Recovery And Climate Experiment (GRACE) mission and will be using the measurement hardware system, such as Ka-band Lunar Gravity Ranging System (LGRS), derived from the GRACE instruments. The primary science objective is to measure and to understand the gravity field, subsurface and interior structure, and thermal evolution of the Moon.

---

[*]Gravity Science Analyst, Outer Planet Navigation Group, Jet Propulsion Laboratory, California Institute of Technology.

[†]Project Co-Investigator, Radio Science Systems Group, Jet Propulsion Laboratory, California Institute of Technology.

[‡]Gravity Science Analyst, Solar Systems Dynamics Group, Jet Propulsion Laboratory, California Institute of Technology.

[§]Project Co-Investigator, Solar Systems Dynamics Group, Jet Propulsion Laboratory, California Institute of Technology.

[¶]Gravity Science Analyst, Orbiter and Radiometric Systems Group, Jet Propulsion Laboratory, California Institute of Technology.

[∥]Project Scientist, GRAIL Mission, Jet Propulsion Laboratory, California Institute of Technology.

There have been a number of gravity campaigns at the Moon previously. Missions, such as Lunar Prospector,[1] provided high-precision lunar gravity fields by processing the conventional Earth-based two-way Doppler measurements. However, due to geometric constraints on Earth-based measurements, the gravity field of Moon's far side had never been directly observed and resulted in much less accuracy in the estimated gravity field. In 2007, JAXA launched a mission called SELenological and ENgineering Explorer (SELENE).[2] SELENE was the first lunar mission to directly observe the far side of the Moon using four-way Doppler tracking. The GRAIL mission is expected to improve the current understanding of the lunar gravity field to an unprecedented level, at least two orders of magnitude improvement, especially for the far-side of the Moon.

After a six-month low-energy transfer to the Moon, the twin spacecraft will be placed in tandem orbits in mid-March and will begin their three-month primary science phase.[3–5] Unlike the GRACE mission, which is equipped with the Global Positioning System (GPS) and accelerometers, the GRAIL spacecraft orbits will be determined by using one-way and inter-satellite Doppler data. Each spacecraft is equipped with an Ultra Stable Oscillator (USO) allowing one-way X-band Doppler tracking with the Earth. The probes are also capable of two-way S-band tracking. During the science phase of the mission, the K-band LGRS will measure the relative range-rate of the probes with high precision while the observed time will be synchronized using the S-band Time Transfer System (TTS). Figure 1 illustrates the GRAIL measurement configuration.
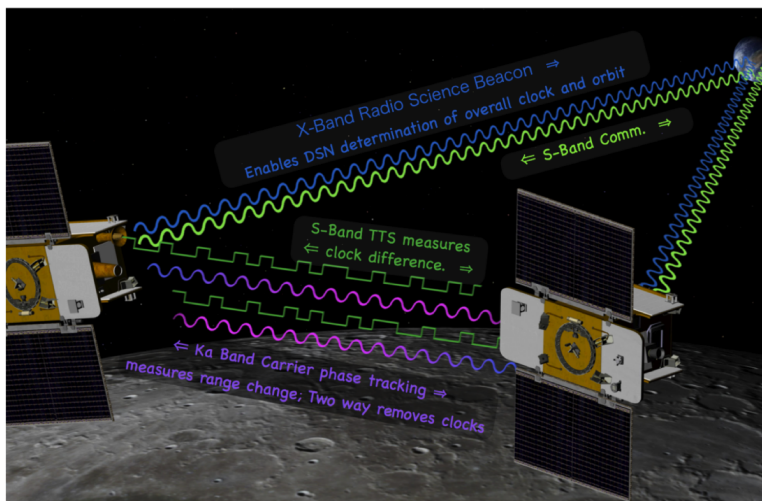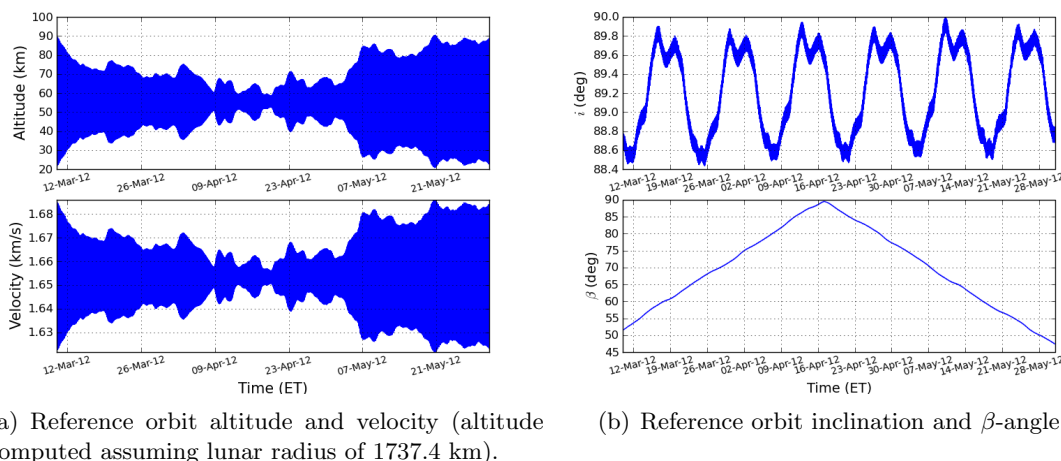

Figure 1. GRAIL Measurement Configuration.

The purpose of this paper is to present the detailed filter setup and estimation technique in processing the GRAIL data. Instead of carrying out only a covariance analysis, which only makes sense if all the error models are correctly implemented, a full-up estimation was considered in order to understand both estimation performance and its statistics. All simulations were carried out using JPL's Multiple Interferometric Ranging And GPS Ensemble (MIRAGE) software set, which will be used to process the actual science data. MIRAGE is a high-precision orbit determination software and was used to process the data from a number of space missions, including Magellan, Lunar Prospector, GRACE, Mars Global

Surveyor, Mars Reconnaissance Orbiter, and many others. One of the most powerful advantage of MIRAGE is the parallelization capability. The current parallel implementation uses Message Passing Interface (MPI) on a cluster system composed of 240 CPU cores.

This paper discusses an overall GRAIL mission capability based on detailed spacecraft dynamics and kinematics models with realistic measurement uncertainties. Also discussed is the effect of various perturbing forces, measurement models, and data arc lengths on overall estimation performance. Among various non-gravitational forces, this study shows that the largest source of non-gravitational error comes from spacecraft thermal radiation. The error contribution due to spacecraft thermal radiation force is characterized with variable *a priori* error constraint model derived from orbit geometry and expected force magnitude. With all error models included, the baseline solution shows that estimating a lunar gravity field is robust against both dynamics and kinematics errors and a nominal field of degree 300 or better can be achieved according to the scaled Kaula rule for the Moon, i.e., $2.5 \times 10^{-4}/n^2$. The core signature, however, is more sensitive to modeling errors and satisfying the science requirement depends on how accurately the spacecraft dynamics can be modeled.

(a) Reference orbit altitude and velocity (altitude computed assuming lunar radius of 1737.4 km).

(b) Reference orbit inclination and β-angle.

Figure 2. GRAIL reference orbit information.

ORBIT GEOMETRY AND RELATIVE ORBIT INFORMATION

Figure 2(a) shows the reference orbit altitude and velocity magnitude of the GRAIL-A spacecraft as functions of the ephemeris time (ET). Note that the GRAIL-A spacecraft is the tailing probe and the GRAIL-B spacecraft is essentially in the same orbit. Considering the lunar reference radius of 1737.4 km, the average altitude is about 55 km. The minimum altitude, when considering an actual lunar topography, is approximately 12 km. Figure 2(b) shows i and β as functions of time, where i represents the inclination and is computed with respect to the lunar pole vector, and β Sun-angle is represented as:

$$\beta = 90° - \cos^{-1}(\hat{\mathbf{e}}_h \cdot \hat{\mathbf{r}}_{sm}), \tag{1}$$

where $\hat{\mathbf{e}}_h$ and $\hat{\mathbf{r}}_{sm}$ represent unit angular-momentum vector and unit Moon-Sun vector, respectively. A high-inclination orbit, but not a perfect polar orbit, is chosen to limit

3

degradation of the estimates for the low-degree gravity coefficients ($n < 20$). A $90°$ β-angle represents that the orbit is normal to the Sun-line, which yields dominating error sources to be along the orbit-normal direction and be constant. Thus, it would be easier to separate the non-gravitational signature from the gravitational effects. The spacecraft starts terminator-crossing at about $\beta = 76°$. For β-angles less than this value, modeling non-gravitational forces becomes much more difficult as the perturbations are changing more rapidly due to part of the orbit being in shadow, and the larger uncertainties degrade especially the lunar core gravitational signature.
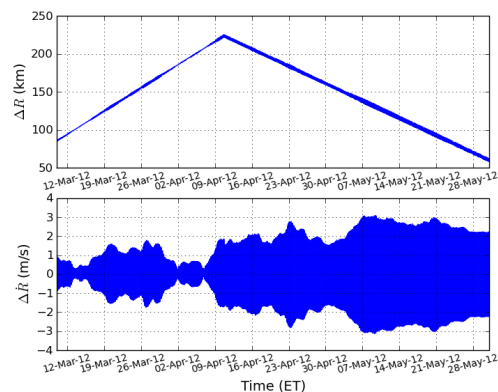
Figure 3.   Relative range and range-rate of the GRAIL-A spacecraft (tailing) with respect to the GRAIL-B spacecraft (leading).
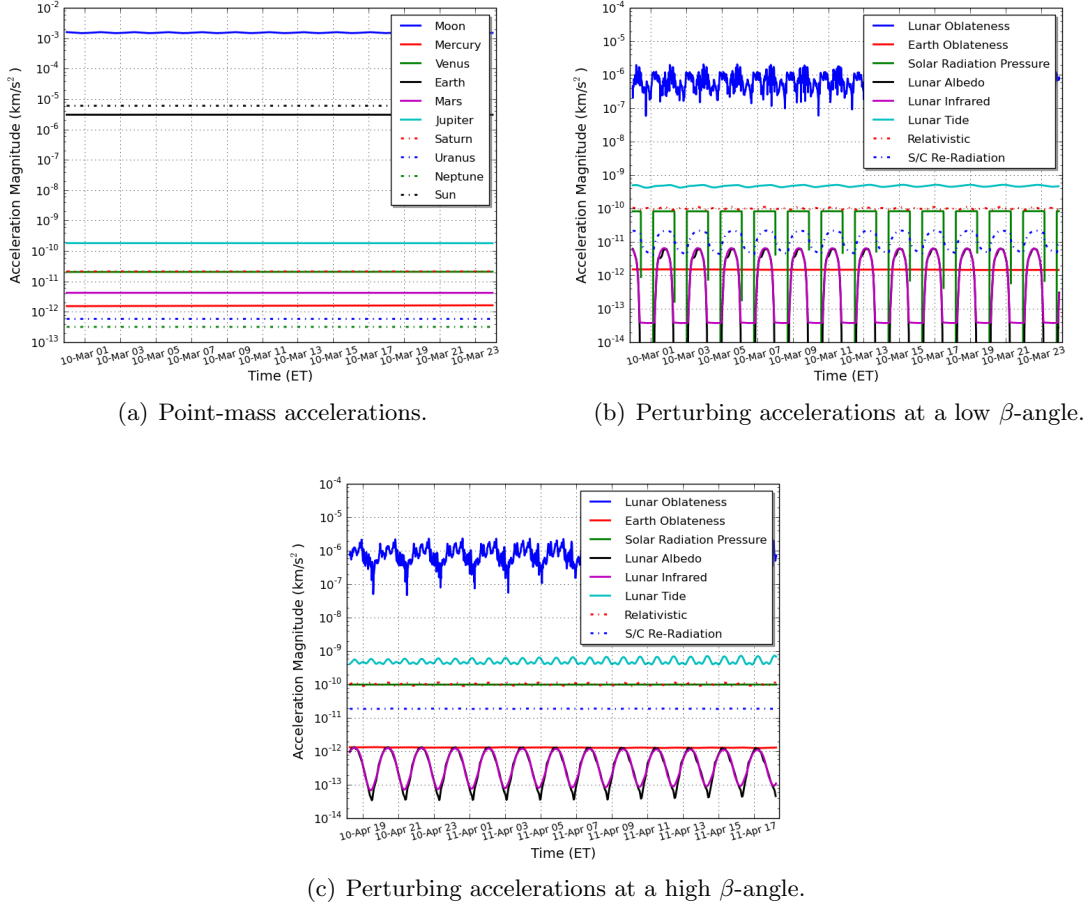
Figure 3 shows the relative range and range-rate of the GRAIL-A spacecraft with respect to the GRAIL-B spacecraft. For estimating long wave-length parameters, such as lunar core signature, a large separation distance is favorable. On the other hand, a small separation distance is favorable for short wave-length parameters, such as high-degree harmonics. The variable separation distance strategy minimizes error increases in the harmonic degrees that are in resonance with the separation distance ($n = 360/(D/30\text{ km})$ where D is the separation distance in km) that occur for constant separation distances. There is a limit on how large the separation distance can be, since at larger distances, multi-path reflections from the lunar surface increase the noise of the LGRS measurements. The LGRS system directly measures the relative range-rate, which is what ultimately contains the gravity signature.

PERTURBING ACCELERATIONS AND THEIR CHARACTERISTICS

For a GRAIL spacecraft, the following acceleration model is considered:

$$\mathbf{a} \;=\; \mathbf{a}_g + \mathbf{a}_{ltc} + \mathbf{a}_{srp} + \mathbf{a}_{str} + \mathbf{a}_{lrp} + \mathbf{a}_{rel} + \mathbf{a}_{misc} + \mathbf{a}_{uf}, \tag{2}$$

where $\mathbf{a}_g$ represents the acceleration due to Newtonian gravity, $\mathbf{a}_{ltc}$ represents the acceleration due to lunar tides and core motion, $\mathbf{a}_{srp}$ represents the acceleration due to solar radiation pressure (SRP), $\mathbf{a}_{str}$ represents the acceleration due to spacecraft thermal radiation, $\mathbf{a}_{lrp}$ represents the acceleration due to lunar radiation pressure, $\mathbf{a}_{rel}$ represents the acceleration due to relativistic effect, $\mathbf{a}_{misc}$ represents the acceleration due to miscellaneous forces, and $\mathbf{a}_{uf}$ represents the acceleration due to un-modeled forces.

(a) Point-mass accelerations.

(b) Perturbing accelerations at a low β-angle.

(c) Perturbing accelerations at a high β-angle.

Figure 4. Accelerations acting on the GRAIL-A spacecraft.

Figure 4 shows the magnitude of the accelerations acting on the GRAIL-A spacecraft. Figure 4(a) shows the point-mass gravitational accelerations due to planetary bodies, which are computed using the DE421 planetary masses and ephemerides. Note that these point-mass accelerations, except for the Moon, are known to the level where their error contributions are negligible in estimating the lunar gravity field. Figures 4(b) and 4(c) show the non-point mass accelerations acting on the GRAIL-A spacecraft at different β-angles. Note that the perturbing accelerations at a high β-angle ($\approx 84°$) are much smoother than the perturbing accelerations at a low β-angle ($\approx 52°$). This smoothness is important for detecting the core signature and will be discussed in detail in the results section.

Acceleration due to the Gravitational Field

Considering the sphericity of the Moon, a spherical harmonics representation of the gravitational potential is considered, which can be stated as:

$$U(\mathbf{r}) \;=\; \frac{GM}{r}\left[1 + \sum_{n=1}^{\infty}\sum_{m=0}^{n}\left(\frac{R_M}{r}\right)^n \left(\bar{C}_{nm}\cos m\lambda + \bar{S}_{nm}\sin m\lambda\right)\bar{P}_{nm}(\sin\phi)\right], \quad (3)$$

where G is the gravitational constant, M is Moon's mass, $r = \|\mathbf{r}\|$ is the Moon-spacecraft distance, λ is the longitude, ϕ is the latitude, R_M is the lunar reference radius, $\bar{C}_{nm}$ and $\bar{S}_{nm}$ are the normalized spherical harmonics, $\bar{P}_{nm}$ is the normalized Legrendre polynomial function, and n and m represent degree and order, respectively. Note that the gravitational potential is defined in the Moon's body-fixed frame. The normalized terms are related to the un-normalized terms as follows:[6]

$$\left(\bar{C}_{nm}, \bar{S}_{nm} \right) = \frac{(C_{nm}, S_{nm})}{N_{nm}}, \tag{4}$$

$$\bar{P}_{nm} = N_{nm} P_{nm}, \tag{5}$$

$$N_{nm} = \sqrt{\frac{(2 - \delta_{0m})(2n + 1)(n - m)!}{(n + m)!}}, \tag{6}$$

where δ_{0m} represents the Kronecker delta. Given the gravitational potential, the acceleration is computed as $\mathbf{a}_g = \partial U / \partial \mathbf{r}$. In this simulation, LP150Q lunar gravity field was used as the nominal field, which was derived using the Lunar Prospector data.[1]

One of the primary science objectives of the GRAIL mission is to estimate a high-resolution gravity field of the moon, which involves estimating from 30,000 to 130,000 spherical harmonics coefficients. The accuracies of the estimated low-degree spherical harmonics and time-varying components depend on how well the remaining accelerations in Eqn.(2) can be modeled, whereas the accuracy of the higher degree terms is mostly proportional to the LGRS measurement accuracy.
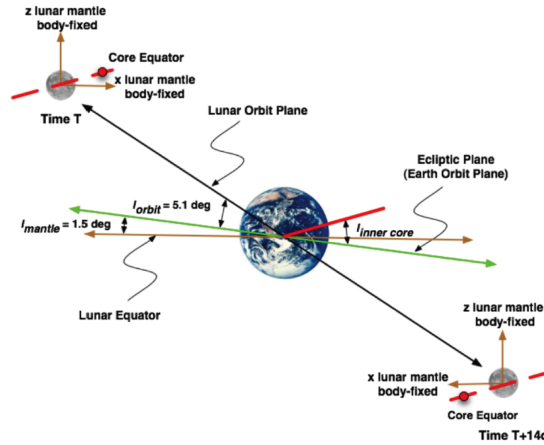

Figure 5. Illustration of Moon's core motion.

Acceleration due to Lunar Core Motion and Lunar Tides

For GRAIL, there are two time-varying components in the lunar gravity field. One is due to the motion of an oblate lunar core relative to the mantle affecting the degree 2 and order 1 spherical harmonics and the other is from the second degree tidal potential changes due to the Earth and Sun. The Moon is believed to have a solid inner core and a fluid outer core.[7,8] The time-varying core signature comes from the monthly motion of the lunar

core equator relative to the lunar body-fixed or mantle frame.[9] Figure 5 shows a cartoon illustrating the Moon's core motion. A point on the core equator (as noted by a red dot) moves relative to the body-fixed equator with a period of one month.

Due to the pole offset of the core and mantle frame, the core motion introduces a monthly signature in the C_{21} and S_{21} gravity coefficients as follows:

$$\Delta \bar{C}_{nm}^{\text{actual}} = \Delta \bar{C}_{nm} + \alpha_{nm} \cos{(\dot{\omega}_m t + \chi_t)}, \tag{7}$$

$$\Delta \bar{S}_{nm}^{\text{actual}} = \Delta \bar{S}_{nm} + \beta_{nm} \cos{(\dot{\omega}_m t + \chi_t)}, \tag{8}$$

where $(\alpha_{nm}, \beta_{nm})$ represent the amplitudes of periodic core signature, $\dot{\omega}_m$ represents the Moon's rotation rate, t represents the time, and χ_t represents a phase offset. The coefficients, Eqns.(7-8), are added to the nominal spherical harmonics to represent the lunar tidal contribution.

The acceleration due to constant lunar tides is modeled using a spherical harmonics representation:

$$\Delta \bar{C}_{nm} - i\Delta \bar{S}_{nm} = \frac{k_{nm}}{2n+1} \sum_j \frac{GM_j}{GM} \frac{R_M^{n+1}}{r_{mj}^{n+1}} P_{nm}(\sin \phi_j) e^{-im\lambda_j}, \tag{9}$$

where k_{nm} is the Love number of degree n and order m, M_j is the mass of the body j (Earth and Sun), ϕ_j is the latitude of the perturbing body j, and r_{mj} is the Moon-body j distance. The current k_2 estimate uncertainty from lunar laser ranging and spacecraft tracking is between 6-8 percent.[8] GRAIL will determine the k_2 Love number to better than 1 percent. It may be possible to detect the third degree Love number if errors in non-gravitational forces are minimal.
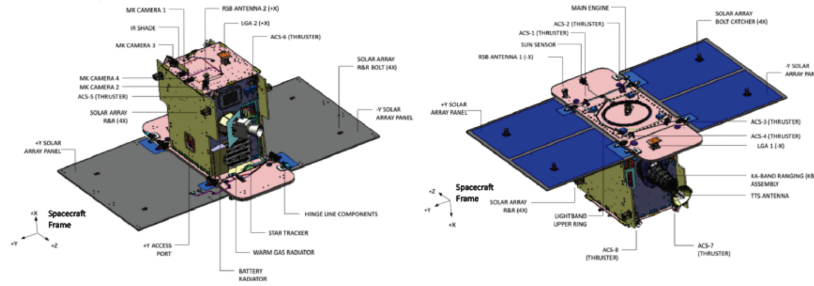

Figure 6. Orbiter configuration for GRAIL-B.

Acceleration due to Solar Radiation Pressure

Figure 6 shows the configuration of the GRAIL-B spacecraft. Note that $-X$ is defined to be along the angular moment vector and $+Y$ is defined to be along nadir. In this paper, each GRAIL spacecraft is modeled with five single-sided flat plates, i.e., three plates for each axis and two for the front and back of the solar arrays, to model the acceleration due

to SRP. For each component, the acceleration is computed as:

$$\mathbf{a}_{srp} = \frac{CS_s}{mr_{sp}^2}\left(F_n\hat{\mathbf{u}}_n + F_r\hat{\mathbf{u}}_s\right), \tag{10}$$

$$F_n = -A\left(2\kappa_d\nu_d + 4\kappa_s\nu_s\cos\alpha\right)\cos\alpha, \tag{11}$$

$$F_r = -A\left(1 - 2\kappa_s\nu_s\right)\cos\alpha, \tag{12}$$

where C is the solar flux constant at one astronautical unit $(1.02 \times 10^8\ \mathrm{kg\cdot km^3/m^2/sec^2})$, m is the spacecraft mass (kg), r_{sp} is the spacecraft-Sun distance (km), S_s is the solar pressure scaling factor (≤ 1), $\hat{\mathbf{u}}_n$ is the unit vector in the direction of the plate normal, $\hat{\mathbf{u}}_s$ is the unit vector from the shape element to the Sun, A is the area of the plate, κ_d is the diffuse reflectivity degradation factor, κ_s is the specular reflectivity degradation factor, ν_d is the diffuse reflectivity coefficient, ν_s is the specular reflectivity coefficient, and α is the angle between the normal of the plate and the shape element to sun unit vector. Note that the best optical material property estimates available at the time of this study were used.

As shown in Figure 4, the acceleration due to SRP is on the order of $10^{-10}\ \mathrm{km/s^2}$. With a ray-tracing technique to model self-shadowing on the spacecraft bus and on-board telemetry of the power system to detect entry and exit from lunar shadow, the SRP accelerations of the GRAIL probes are expected to be determined to a few percent level. One important item to note is that the effects due to SRP and gravity are fundamentally different and are separable in the estimation process.

Acceleration due to Spacecraft Thermal Radiation

For a flat plate component, the acceleration due to spacecraft thermal radiation can be computed as:

$$\mathbf{a}_{str} = \frac{-2 \times 10^{-6} A\sigma_{sb}}{3mc}\epsilon T^4\hat{\mathbf{u}}_n, \tag{13}$$

where σ_{sb} is the Stefan-Boltzmann constant $(5.6704\times10^{-8}\ \mathrm{W/m^2/K^4})$, c is the speed of light $(3\times10^5\ \mathrm{km/s})$, ϵ is the surface emissivity, and T is the surface temperature (K).

For computing the spacecraft thermal radiation acceleration, each GRAIL spacecraft was modeled using 28 flat-plate surfaces and the area-averaged temperature as a function of time for each surface, spanning one orbital period, are derived from node temperature outputs of the detailed thermal finite-element modeling of both spacecraft performed by Lockheed Martin using the Thermal Desktop software. Due to the complexity of running a full thermal model, the temperature profiles were computed for the three different β angles, i.e., $49°$, $77°$, and $90°$. Note that $\beta = 77°$ is approximately when spacecraft terminator-crossing starts. Again, the best material optical property estimates available at the time of this study were used.

Figure 7(a) shows the predicted acceleration due to spacecraft thermal radiation during the entire science phase in the spacecraft frame. Note that, for GRAIL-A spacecraft, $-X$ is defined to be along the angular moment vector and $-Y$ is defined to be along nadir. The acceleration over an orbit is computed for the three different β angles and is interpolated as a function of β-angle and an angle from the Moon's equator. In the actual gravity reconstruction, the surface temperature uncertainty is expected to be less than 5 K. Figure 7(b)
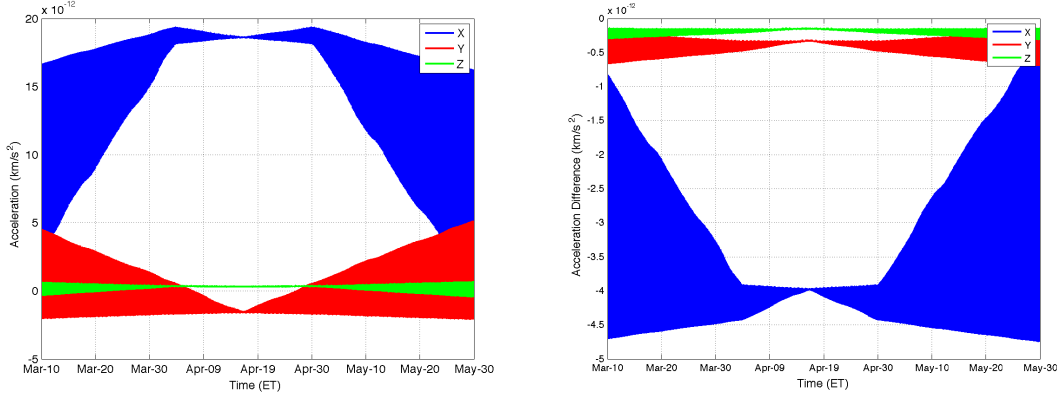
(a) Acceleration due to thermal radiation force from the GRAIL-A spacecraft.

(b) Acceleration difference between the nominal and +5 K biased cases for the GRAIL-A spacecraft.

Figure 7. Acceleration due to spacecraft thermal radiation force.

shows the acceleration difference between the nominal and a case with the temperature of all surfaces pushing towards each positive body-frame direction biased by +5 K. Note that most of the error is expected to be along the SRP direction.

Acceleration due to Lunar Radiation

The element of acceleration on a spacecraft due to lunar radiation pressure from a point P on the surface of the Moon can be computed as:

$$d\mathbf{a}_{lrp} = H\left(F_n \hat{\mathbf{u}}_n + F_r \hat{\mathbf{r}}_{ps}\right) \frac{\cos \psi}{\pi r_{ps}^2} dA_{planet}, \tag{14}$$

where for reflected sunlight (albedo):

$$H = \frac{CS_m \cos \psi_s}{mr_{ms}^2} \sum_{\ell=0}^{N} \sum_{m=0}^{\ell} \left(C_{\ell m}^A \cos m\lambda_p + S_{\ell m}^A \sin m\lambda_p\right) P_{\ell m}(\sin \phi_p), \tag{15}$$

and for thermal emission (infrared):

$$H = \frac{C}{4mr_{ms}^2} \sum_{\ell=0}^{N} \sum_{m=0}^{\ell} \left(C_{\ell m}^E \cos m\lambda_p + S_{\ell m}^E \sin m\lambda_p\right) P_{\ell m}(\sin \phi_p), \tag{16}$$

where r_{ms} is the Moon-Sun distance, S_m is lunar radiation pressure scaling factor (≤ 1), $\phi_p and \lambda_p$ are the latitude and longitude of the point P, $P_{\ell m}$ is the associated Legendre function, r_{ps} is the point P to spacecraft distance, $\hat{\mathbf{r}}_{ps}$ is the point P to spacecraft direction, ψ_S is the Sun-Moon-point P angle, ψ is the angle between the Moon-point P and point P-spacecraft direction vectors, and $(C_{\ell m}^A, S_{\ell m}^A)$ and $(C_{\ell m}^E, S_{\ell m}^E)$ are spherical harmonics for the albedo and thermal maps, respectively. The acceleration due to reflected sunlight was computed using the Delft Lunar Albedo Model 1 (DLAM-1), i.e., $(C_{\ell m}^A, S_{\ell m}^A)$, which was derived from Clementine imagery.[10] A different albedo map, derived internally at JPL, was compared with DLAM-1 and essentially the same result was obtained.

9
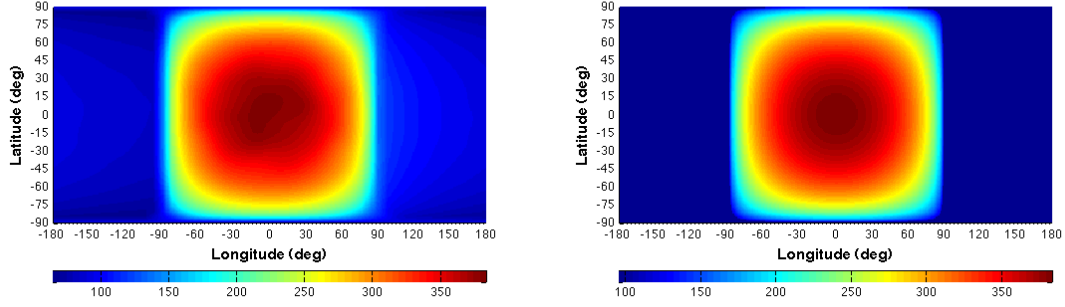
(a) Observed lunar temperature map.

(b) Simple lunar temperature map where $T = T_{max}(\cos \psi_S)^{1/4}$ for $\leq 89.5°$ and $T = T_{min}$ otherwise.
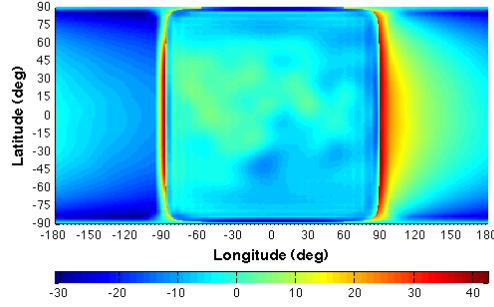
(c) Lunar temperature map difference.

Figure 8. Temperature map of the Moon at the local noon time.

Note that the albedo map is a constant field whereas the thermal map is a function of local lunar time because of topographic variation. For this reason, the following simple thermal emission model was derived for this simulation:

$$H = \begin{cases} \dfrac{C\sigma_{sb}T_{max}^4 \cos \psi_S}{4mr_{cs}^2 L} & \text{, if } \psi_S \leq 89.5° \\[2ex] \dfrac{C\sigma_{sb}T_{min}^4}{4mr_{cs}^2 L} & \text{, otherwise} \end{cases}, \qquad (17)$$

where T_{max}=382.86 K and T_{min}=95 K. Figure 8 shows the thermal maps computed at the local noon time, i.e., Sun is at 0° longitude and 0° latitude. Figure 8(a) shows a thermal map derived using the measurements from Lunar Reconnaissance Orbiter's Diviner Lunar Radiometer Experiment data. Figure 8(b) shows the simple map which essentially represents Eqn.(17), i.e., a billiard-ball thermal model. Figure 8(c) shows the difference between the two thermal maps and a very small difference is observed except for near $\lambda = \pm 90°$. A more sophisticated model is planned to be used in processing the actual data.

10

For the Moon, as shown in Figure 4, the accelerations due to reflected sunlight and thermal emission are on the same order and behave similarly. Note that the simple thermal model was used to compute the acceleration due to thermal emission in this study.

Acceleration due to General Relativity

The acceleration due to general relativity is modeled using the parameterized post-Newtonian (PPN) formulation.[11,12] As shown in Figure 4, the nominal acceleration due to point-mass general relativity is on the order of 10^{-10} km/s^2; however, this acceleration is acting mostly in the radial direction and the accelerations in the along-track and cross-track are about two orders of magnitude smaller. Considering the current accuracies of the PPN parameters, γ and β, the uncertainty in relativistic acceleration is less than 0.1 percent. This yields acceleration less than 1×10^{-15} km/s^2 in along-track direction, which is beyond GRAIL's capability (i.e., 1 micron/s at 5-second count time).

Acceleration due to Miscellaneous Forces

The miscellaneous forces consist of small accelerations such as spacecraft out-gassing and propulsion leaks. For the GRAIL mission, the acceleration due to out-gassing is expected to be about 6.25×10^{-13} km/s^2 during early and late science phase and 2.5×10^{-13} km/s^2 during mid-science phase. The acceleration due to gas leak is expected to be about 10^{-14} km/s^2. Note that the acceleration due to miscellaneous forces are not modeled in trajectory integration, but their contribution is estimated as a part of the periodic acceleration of the next section.

Acceleration due to Un-Modeled Forces

The acceleration due to un-modeled forces is used to represent the errors in the non-gravitational forces from solar pressure, spacecraft thermal radiation, lunar radiation, and spacecraft outgassing. For GRAIL gravity reconstruction, the un-modeled acceleration is represented as the following periodic acceleration formulation:

$$
\begin{aligned}
\mathbf{a}_{uf} \quad = \quad & (P_r + C_{r1} \cos\theta + C_{r2} \cos 2\theta + S_{r1} \sin\theta + S_{r2} \sin 2\theta)\, \hat{\mathbf{e}}_r \\
& + (P_t + C_{t1} \cos\theta + C_{t2} \cos 2\theta + S_{t1} \sin\theta + S_{t2} \sin 2\theta)\, \hat{\mathbf{e}}_t \\
& + (P_n + C_{n1} \cos\theta + C_{n2} \cos 2\theta + S_{n1} \sin\theta + S_{n2} \sin 2\theta)\, \hat{\mathbf{e}}_n,
\end{aligned}
\tag{18}
$$

where $\hat{\mathbf{e}}_r = \mathbf{r}/\|\mathbf{r}\|$, $\hat{\mathbf{e}}_n = (\mathbf{r} \times \mathbf{v})/\|\mathbf{r} \times \mathbf{v}\|$, and $\hat{\mathbf{e}}_t = \hat{\mathbf{e}}_n \times \hat{\mathbf{e}}_r$. Here, θ denotes the angle from the ascending node of the spacecraft orbit on the EME2000 plane to the spacecraft. The periodic acceleration is nominally set to zero in the initial trajectory integration and is used to estimate the errors in the non-gravitational accelerations. The terms P_i represent the constant accelerations during the time interval which the corresponding periodic acceleration model is active. The terms (C_{i1}, S_{i1}) and (C_{i2}, S_{is}) represent the once-per-orbit and twice-per-orbit acceleration amplitudes, respectively.
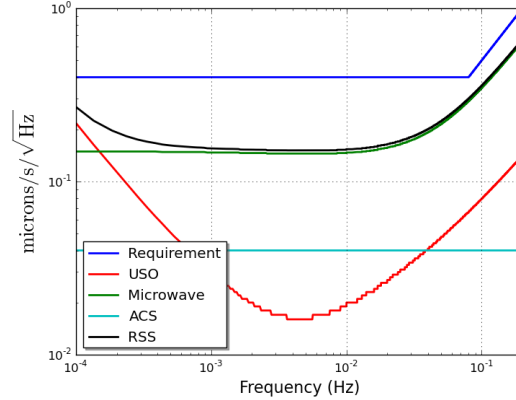
MEASUREMENT MODEL

In GRAIL gravity reconstruction, two different measurement types are considered. The first data type is the conventional Earth-based Deep Space Network (DSN) Doppler tracking,

i.e.,

$$z_d \;\; = \;\; \hat{\boldsymbol{\rho}}_{se} \cdot \dot{\boldsymbol{\rho}}_{se}, \tag{19}$$

where $\boldsymbol{\rho}_{se}$ represents the vector from an Earth tracking station to the spacecraft. The one-way Doppler data is assumed to have $\sigma_d = 0.05$ mm/s uncertainty at 10-second count time. The baseline case assumes that GRAIL-A is tracked only from Goldstone complex and GRAIL-B is tracked only from Canberra complex whenever the spacecraft is in view.

Figure 9. Root power spectral density of the KBRR noise.

The second data type is the LGRS measurement. Both inter-satellite Ka-band range (KBR) and K-band range-rate (KBRR) measurements are available, but because it is cumbersome to establish range bias estimates at cycle slip boundaries, only the range-rate is considered. The inter-satellite range-rate measurement is represented as:

$$z_s \;\; = \;\; \hat{\boldsymbol{\rho}}_{ba} \cdot \dot{\boldsymbol{\rho}}_{ba}, \tag{20}$$

where $\boldsymbol{\rho}_{ba}$ represents the vector from GRAIL-A to GRAIL-B. The inter-satellite range-rate data is assumed to have $\sigma_s = 1$ μm/s uncertainty at 5-second count time. Figure 9 shows the root power spectral density plot of KBRR noise, showing margin against the science requirement (solid blue curve). The error contributions due to dominating noise sources, such as USO, microwave, and attitude control system, are also shown. In terms of acceleration, the inter-satellite measurement accuracy yields 2×10^{-10} km/s^2=0.002 mGal.

Note that these measurement models are only approximates of the actual measurement formulation. The details of the GRAIL measurement model are beyond the scope of this paper.

GRAIL SCIENCE REQUIREMENTS

There are six science investigations for the GRAIL mission that constitute mission success.

1. *Crust and Lithosphere*: Determine the Moon's global gravity field with global average surface resolution of 30 km and with an accuracy of ± 10 mGal (global requirement).

2. *Thermal Evolution*: Determine large regional gravity with global average surface resolution of 30 km and with an accuracy of ± 2 mGal (regional requirement).

3. *Impact Basins*: Determine small regional gravity that resolves basins and rings to a global average surface resolution of 30 km to a precision of ± 0.5 mGal.

4. *Crustal Brecciation and Magmatism*: Determine high-resolution local gravity fields with global average surface resolution of 30 km to a precision of ± 0.1 mGal.

5. *Deep Interior*: To constrain the deep interior from tides, determine the Love Number, k_2, to an accuracy of 6×10^{-4}.

6. *Core Detection*: To place limits on the size of a possible solid inner core, determine the Love Number, k_2, to an accuracy of 2×10^{-4} and determine the second degree and first-order gravity coefficients to an accuracy of 1×10^{-10}.

Satisfying all six investigations will constitute baseline mission success, whereas satisfying the first four will constitute minimum mission success. The investigations 1 and 2 depend on the estimated high-resolution gravity field. The investigations 3 and 4 depend on the LGRS measurement accuracy. Lastly, the investigation 5 depends on the estimation of k_2 whereas the investigation 6 depends on the estimation of k_2 and α_{21}.

LEAST-SQUARES FILTER TECHNIQUE

Gravity field reconstruction is based on the least-squares estimation principle.[13] Define the cost function J as follows:

$$J(\mathbf{x}_0) = \frac{1}{2}(\mathbf{x}_0 - \mathbf{x}_a)^T \mathbf{\Lambda}_a (\mathbf{x}_0 - \mathbf{x}_a) + \frac{1}{2}[\mathbf{z}^* - \mathbf{z}(\mathbf{x}_0)]^T \mathbf{W}[\mathbf{z}^* - \mathbf{z}(\mathbf{x}_0)], \qquad (21)$$

where $\mathbf{x}_a$ is the *a priori* estimate vector, $\mathbf{\Lambda}_a$ is the *a priori* information matrix, $\mathbf{z}^*$ is the actual measurement vector (i.e., observed data), $\mathbf{z}$ is the predicted measurement vector, $\mathbf{W}$ is the measurement weight matrix, and $\mathbf{x}_0$ is the estimate vector. By applying the necessary conditions to Eqn.(21) and by linearizing about the nominal trajectory, $\bar{\mathbf{x}}_0$, the following normal equation is obtained:

$$\underbrace{\left[\mathbf{\Lambda}_a + \mathbf{H}_{\mathbf{x}_0}^T \mathbf{W} \mathbf{H}_{\mathbf{x}_0}\right]}_{\mathbf{\Lambda}_0} \delta\mathbf{x}_0 = \underbrace{\mathbf{\Lambda}_a \delta\mathbf{x}_a + \mathbf{H}_{\mathbf{x}_0}^T \mathbf{W} \Delta\mathbf{z}}_{\tilde{\mathbf{z}}}, \qquad (22)$$

where $\delta\mathbf{x}_a = \mathbf{x}_a - \bar{\mathbf{x}}_0$, $\Delta\mathbf{z} = \mathbf{z}^* - \mathbf{z}(\bar{\mathbf{x}}_0)$, and

$$\mathbf{H}_{\mathbf{x}_0} = \left. \frac{\partial \mathbf{z}}{\partial \mathbf{x}_0} \right|_{\mathbf{x}_0 = \bar{\mathbf{x}}_0} = \begin{bmatrix} \mathbf{h}_1 \mathbf{\Phi}_1 \\ \vdots \\ \mathbf{h}_N \mathbf{\Phi}_N \end{bmatrix}. \qquad (23)$$

Here, $\mathbf{\Lambda}_0$ is called the epoch-state information matrix, $\tilde{\mathbf{z}}$ is called the data vector, and $\mathbf{\Phi}_k = \mathbf{\Phi}(t_k, t_0)$ is the usual state transition matrix mapping the deviation from t_0 to t_k. Once the epoch-state information matrix is computed, the epoch-state covariance matrix can be obtained by computing $\mathbf{P}_0 = \mathbf{\Lambda}_0^{-1}$. The least-squares filter is an iterative method

where the correction vector $\delta\mathbf{x}_0$ is computed until the solution converges to some user-defined quantities, e.g., $||\delta\mathbf{x}_0|| < \epsilon_{\delta\mathbf{x}_0}$. In the actual filtering process, MIRAGE utilizes the Square-Root Information Filter (SRIF) technique in order to retain numerical precision.[13]

When solving for a large number of parameters, the convergence is very sensitive to the *a prior* values and uncertainties. For example, if the spacecraft initial state is poorly known, the iteration may never converge if the filter tries to solve for both the trajectory and a high-resolution gravity field at the same time. In order to avoid this problem, the *local* parameters are first estimated, and once a solution is obtained, the *global* parameters are estimated.

For each spacecraft, the local parameters consist of the spacecraft initial state, the solar radiation pressure scale factor, two constant SRP scaling terms orthogonal to the spacecraft-to-Sun vector, fifteen periodic acceleration terms for every two hours, four inter-satellite range-rate measurement correction terms for every two hours, and Earth-based Doppler bias and drift rate. The global parameters consist of three inter-satellite range-rate time-tag biases, degree 2 and 3 Love numbers, degree 2 and order 1 amplitudes of periodic tidal signature, Moon's GM, and a 150×150 gravity field (approximately 23,000 parameters). The time-tag biases represent the offset between the DSN time system and the KBRR time-tag which is derived from the spacecraft clock.

In general, it would be ideal to process the entire science phase data at once and preserve the long wave-length signature. However, there are planned angular momentum desaturations (AMD) which essentially breaks the information. Moreover, there is a numerical limitation on how long a trajectory can be integrated without introducing numerical noise in the estimates. In order to avoid this problem, the science phase trajectory is divided whenever an AMD occurs. This study assumes that an AMD occurs every 2 days which yields 42 total arcs.

For each 2-day arc, first the local parameters are estimated until a convergence is achieved. Secondly, using MIRAGE's parallel processing capability, a SRIF array for both local and global parameters of each arc is computed, which is the most numerically intensive process. Lastly, all SRIF arrays are accumulated and inverted to compute the correction vector. The last two steps are repeated until the global solution converged.

SIMULATION RESULTS

In the baseline study, DSN and KBRR measurements are simulated using a truth case where Eqn.(2) is integrated with all models turned on and by generating measurements according to a realistic tracking schedule and uncertainties. Note that inter-satellite truth measurements are generated using a colored-noise spectrum ranging from 0.4 μm/s (long-wave-length) to 1 μm/s (short wave-length). This noise spectrum accounts for the error contributions from USO and spacecraft attitude jitter (see Figure 9). The baseline nominal trajectory is setup identical to the truth case with the *a priori* uncertainty model given in Table 1.

It would be ideal to model every single non-gravitational effect in gravity reconstruction, but this is practically impossible as, in most cases, there isn't enough information for such modeling. Instead, a periodic acceleration model is chosen to represent these un-modeled accelerations. Deriving an *a priori* periodic acceleration model is one of the most critical

Table 1. *A priori* uncertainty model.

Parameter	*A priori* Uncertainty
Position	1000 km in each direction
Velocity	1 m/s in each direction
Overall SRP scaling factor	10 %
Orthogonal SRP scaling factors	2 % in each direction
Doppler correction terms	widely open
LGRS correction terms	widely open
Periodic acceleration	variable
Lunar gravity field	LP150Q solution
k_2, α_{21} and β_{21}	widely open

parts in the GRAIL gravity reconstruction as it's directly related to the formal uncertainties of the estimated low-degree gravity field and time-varying core signature. In order to derive a proper *a priori* model, the effect due to all non-gravitational acceleration is analyzed. The potential error contribution due to all the non-gravitational forces is represented using the *a priori* periodic acceleration model.
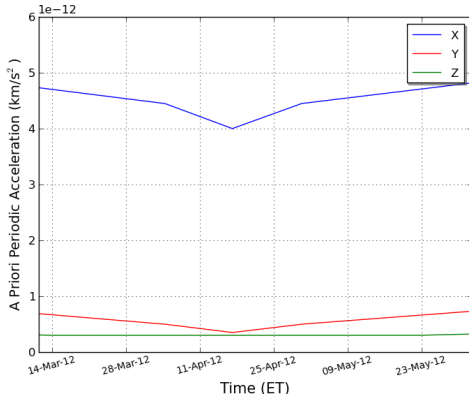
(a) Constant terms.
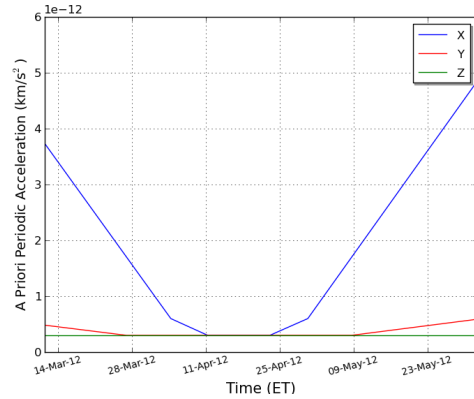
(b) Once/orbit and twice/orbit terms.

Figure 10. *A priori* periodic acceleration with 3×10^{-13} km/s^2 minimum acceleration.

The error due to spacecraft thermal radiation force is expected to be bounded by changes in spacecraft temperature of less than 5 K as shown in Figure 7(b). For this reason, the constant periodic acceleration error is chosen to follow the upper bound of the acceleration difference shown in Figure 7(b). The once per orbit and twice per orbit terms are chosen to be the difference between the upper and lower bounds of this acceleration difference. For all the periodic acceleration *a priori* terms, the absolute minimum is chosen to be 3×10^{-13} km/s^2 and this *a priori* model is shown in Figure 10. To be more specific, for each 2-day arc, the *a priori* periodic acceleration is initialized according to these profiles. It is important to note that the uncertainty due to all the other non-gravitational forces is bounded by this *a priori* periodic acceleration model as well.
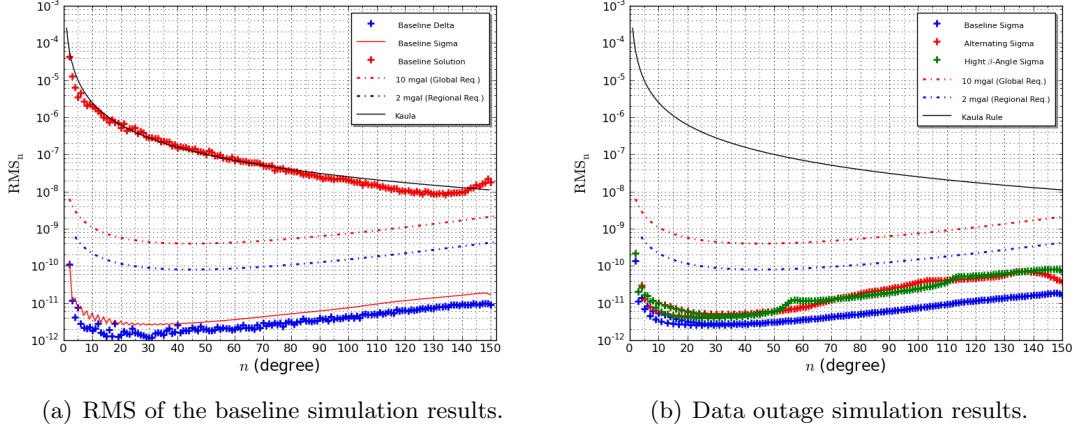
(a) RMS of the baseline simulation results.   (b) Data outage simulation results.

Figure 11.   RMS of the simulation results.

Table 2.   Baseline core-signature estimates.

	$\Delta_{k2} \times 10^4$	$\sigma_{k2} \times 10^4$	$\Delta_{\alpha21} \times 10^{10}$	$\sigma_{\alpha21} \times 10^{10}$	$\Delta_{\beta21} \times 10^{11}$	$\sigma_{\beta21} \times 10^{11}$
Req.		2.00		1.00		2.50
Baseline	0.93	0.94	0.62	0.67	-2.01	1.77

Figure 11(a) shows the root-mean-square (RMS) of the estimated gravity field (solution), corresponding 1-σ formal uncertainties (sigma), and the difference between the truth and estimated gravity fields (delta). Also shown are the global and regional science requirement plots and predicted Moon's Kaula rule. The Kaula rule is assumed to be $2.5 \times 10^{-4}/n^2$. Note that the RMS_n is defined as:

$$\text{RMS}_n = \sqrt{\frac{\sigma_n^2}{2n+1}}, \tag{24}$$

where $\sigma_n^2 = \sum_{m=0}^{n} \left(C_{nm}^2 + S_{nm}^2 \right)$ is called the degree variance.

A few important observations can be made from Figure 11(a). First, the difference between the truth and estimated gravity fields is smooth and is bounded by the formal uncertainty. This indicates a correct filter setup and a stable filter solution. Second, both the global and regional science requirements are satisfied with the baseline assumptions. Lastly, the colored measurement noise, i.e., instrument error, is well-bounded by the white noise assumption. The linear extrapolation of the estimated uncertainties gives that a nominal gravity field of degree 300 or better can be determined according to the Kaula rule.

Table 2 shows the estimates of the core signature terms, where Δ_i represents the difference between the truth and the estimated parameter i and σ_i represents the estimated 1-σ uncertainty of parameter i. The result shows that science investigations 5 and 6 can also be satisfied under the baseline assumptions, but with relatively tight error margin.

Table 3 shows the effect of data outage for both Doppler and inter-satellite data. The *alternating* case represents what happens if data outage occurs for every other arc, which

Table 3. Effect of data outage.

Cases	$\sigma_{k2} \times 10^4$	$\sigma_{\alpha 21} \times 10^{10}$	$\sigma_{\beta 21} \times 10^{11}$
Baseline	0.94	0.67	1.77
Alternating[a]	1.41	1.06	3.17
High β-Angle[a]	1.48	1.05	3.04
Alternating[b]	1.80	1.33	3.81
High β-Angle[b]	1.93	1.36	4.00

a. Minimum *a priori* periodic acceleration $= 3 \times 10^{-13}$ km/s^2.
b. Minimum *a priori* periodic acceleration $= 1 \times 10^{-12}$ km/s^2.

yields a total of 24 arcs. The *high β-angle* case represents what happens if only the middle 28 days are considered in gravity reconstruction, which yields a total of 14 arcs. Note that the 2-day arc length remains the same. The result shows that the science requirement on k_2 can still be achieved whereas the requirement on α_{21} cannot be achieved.

Figure 11(b) shows the estimated formal uncertainty of the data outage study. Both the global and local requirements are satisfied, but the *alternating* and *high β-angle* cases resulted in a five-times higher uncertainty in the estimated high-degree spherical harmonics.

All cases simulated in this study have shown to satisfy the science requirements that constitute minimum science success. Thus, the rest of this section only discusses the results of the core-signature estimates, the toughest of the science requirements to satisfy. Also, only the formal uncertainty is discussed throughout this paper as the estimated solution is well characterized by the formal error.

Table 4. Effect of minimum *a priori* periodic accelerations.

Cases	$\sigma_{k2} \times 10^4$	$\sigma_{\alpha 21} \times 10^{10}$	$\sigma_{\beta 21} \times 10^{11}$
Baseline	0.94	0.67	1.77
5×10^{-13} km/s^2	1.04	0.73	1.90
1×10^{-12} km/s^2	1.13	0.81	2.25
5×10^{-12} km/s^2	1.46	1.12	5.36

As shown in Figure 10, the baseline case assumed the minimum *a priori* periodic acceleration of 3×10^{-13} km/s^2. Table 4 shows the effect of varying the minimum *a priori* periodic acceleration. Under the nominal mission scenario, e.g., no data outage, normal spacecraft function, etc., the realistic error is expected to be somewhere between 5×10^{-13} km/s^2 and 1×10^{-12} km/s^2. The results shows that the baseline science success can be achieved considering the minimum *a priori* acceleration less than 1×10^{-12} km/s^2, but with very tight error margin.

Table 5 shows the effect of different data arc lengths, i.e., AMD separations. As expected, the formal uncertainty becomes smaller as the arc length increases. The baseline case assumed a 2-day arc, but in practice, the arc length is expected to be longer. In all cases, except for the 1-day arc length with minimum *a priori* periodic acceleration of 1×10^{-12} km/s^2, all science requirements are satisfied, but again, with very tight error

Table 5. Effect of data arc length.

Cases	$\sigma_{k2} \times 10^4$	$\sigma_{\alpha21} \times 10^{10}$	$\sigma_{\beta21} \times 10^{11}$
1 day[a]	1.11	0.80	2.60
Baseline	0.94	0.67	1.77
3 day[a]	0.89	0.64	1.66
4 day[a]	0.85	0.61	1.33
5 day[a]	0.82	0.58	1.23
1 day[b]	1.46	1.02	3.10
2 day[b]	1.13	0.81	2.25
3 day[b]	1.07	0.77	2.09
4 day[b]	1.01	0.73	1.82
5 day[b]	0.98	0.70	1.73

a. Minimum *a priori* periodic acceleration $= 3 \times 10^{-13}$ km/s^2.
b. Minimum *a priori* periodic acceleration $= 1 \times 10^{-12}$ km/s^2.

margin.

Table 6. Effect of DSN tracking schedule

Cases	$\sigma_{k2} \times 10^4$	$\sigma_{\alpha21} \times 10^{10}$	$\sigma_{\beta21} \times 10^{11}$
Baseline	0.94	0.67	1.77
24 hour[a]	0.73	0.52	1.44
12 hour[a]	0.83	0.59	1.61
8 hour[a]	0.90	0.64	1.75
24 hour[b]	0.84	0.60	1.90
12 hour[b]	0.97	0.68	2.06
8 hour[b]	1.08	0.76	2.21

a. Minimum *a priori* periodic acceleration $= 3 \times 10^{-13}$ km/s^2.
b. Minimum *a priori* periodic acceleration $= 1 \times 10^{-12}$ km/s^2.

The baseline case assumed that the GRAIL-A spacecraft is tracked by the Goldstone complex and the GRAIL-B spacecraft is tracked by the Canberra complex whenever the spacecraft is in view. This scenario yields a little more than 8 hours of tracking per spacecraft per day. Table 6 shows the resulting core-signature estimates for different tracking schedules. N-hour tracking means that each GRAIL spacecraft is tracked from DSN stations exactly N hours per day. Note that the 8-hour case with minimum *a priori* periodic acceleration of 3×10^{-13} km/s^2 shows an improvement over the baseline case although there are less DSN tracking data. This is because each spacecraft tracking schedule is distributed among multiple DSN stations, which provides additional orbit information due to geometric parallax.

The nominal mission assumes an X-band tracking with $\sigma_d = 0.05$ mm/s uncertainty at 10-second count time. Assuming the on-board X-band transmitter fails, two-way S-band tracking is possible with $\sigma_d = 0.5$ mm/s uncertainty at 10-second count time. Table 7

Table 7. Effect of X-band tracking failure.

Cases	$\sigma_{k2} \times 10^4$	$\sigma_{\alpha21} \times 10^{10}$	$\sigma_{\beta21} \times 10^{11}$
Baseline	0.94	0.67	1.77
S-band GRAIL-A	1.03	0.74	2.27
S-band GRAIL-B	1.01	0.72	2.36

shows the effect of on-board X-band transmitter failure. The result shows that the baseline mission success can be achieved even with S-band tracking.

Table 8. Effect of kinematics errors.

Cases	$\Delta_{k2} \times 10^4$	$\Delta_{\alpha21} \times 10^{10}$
Temperature Control	0.05	0.01
Time-Tag Error	0.02	0.02
Attitude Pointing Error	0.20	0.10

Table 8 shows the effect of kinematics errors on the estimated core parameters. Note that Table 8 shows the error in the estimated parameters, which essentially represent the effect due to kinematic errors. The formal uncertainties are the same as the baseline case. The *temperature control* case shows the effect of the error in the LGRS measurement frequency and signal path-length due to thermal variation. The *time-tag error* shows the effect of initial time-tag offset of 100 ms. Lastly, the *attitude pointing error* shows the effect of a 3-σ single-spacecraft attitude pointing error, which translates to about 0.06 μm/s on LGRS data.

CONCLUSIONS

This paper presented a detailed sensitivity analysis of estimating a high-resolution lunar gravity field and time-varying core signature using the measurements from the GRAIL mission. All the perturbing forces affecting the spacecraft dynamics are discussed in detail and a proper *a priori* error constraint model for the non-gravitational accelerations was derived based on the expected errors in the spacecraft thermal radiation force. Moreover, a detailed filter setup and estimation technique for the actual GRAIL mission is presented.

Considering a realistic tracking schedule and measurement uncertainties, the baseline simulation showed that baseline mission success can be achieved, but with relatively tight error margin for the time-varying core-signature terms. Moreover, the result shows that estimating a lunar gravity field is robust against both dynamics and kinematics errors and a nominal field of degree 300 or better can be determined according to the scaled Kaula rule for the Moon, i.e., $2.5 \times 10^{-4}/n^2$, and assuming the nominal mission plan. Also discussed are the effects of data outage, minimum *a priori* periodic accelerations, data arc length, DSN tracking schedule, X-band tracking failure, and kinematics errors. In all simulated cases, the minimum science success was achieved, but the accuracy of time-varying core terms are highly sensitive to the dynamics error and tracking plan.

ACKNOWLEDGEMENTS

REFERENCES

[1] A. Konopliv, S. Asmar, and D.-N. Yuan, "Recent gravity models as a result of the Lunar Prospector mission," *Icarus*, Vol. 150, 2001, pp. 1–18.

[2] K. Matsumoto, S. Goossens, Y. Ishihara, Q. Liu, F. Kikuchi, T. Iwata, N. Namiki, H. Noda, H. Hanada, N. Kawano, F. G. Lemoine, and D. D. Rowlands, "An improved lunar gravity field model from SELENE and historical tracking data: Revealing the farside gravity features," *Journal of Geophysical Research*, Vol. 115, No. E06007, 2010.

[3] R. Roncoli and K. Fujii, "Mission Design Overview for the Gravity Recovery and Interior Laboratory (GRAIL) Mission," *AIAA Guidance, Navigation, and Control Conference*, August, 2010, Toronto, Ontario Canada. AIAA 2010-8383.

[4] M.-K. J. Chung, "Trans-Lunar Cruise Trajectory Design of GRAIL (Gravity Recovery and Interior Laboratory) Mission," *AIAA Guidance, Navigation, and Control Conference*, August, 2010, Toronto, Ontario Canada. AIAA 2010-8384.

[5] S. Hatch, R. Roncoli, and T. Sweetser, "GRAIL Trajectory Design: Lunar Orbit Insertion through Science," *AIAA Guidance, Navigation, and Control Conference*, August, 2010, Toronto, Ontario Canada. AIAA 2010-8385.

[6] W. Kaula, *Theory of Satellite Geodesy Applications of Satellites to Geodesy.* Dover Publications, 2000.

[7] R. Weber, P.-Y. Lin, E. Garnero, Q. Williams, and P. Lognonne, "Seismic Detection of the Lunar Core," *Science*, Vol. 331, No. 6015, 2011, pp. 309–312.

[8] J. Williams, D. Boggs, and J. Ratcliff, "Lunar Moment of Inertia and Love Number," *42nd Lunar and Planetary Science Conference*, March 2011, The Woodlands, Texas. No. 2610.

[9] J. Williams, "A scheme for lunar inner core detection," *Geophysical Research Letters*, Vol. 34, No. L03202, 2007.

[10] R. Floberghagen, P. Visser, and F. Weischede, "Lunar Albedo Force Modeling and its Effect on Low Lunar Orbit and Gravity Field Determination," *Advances in Space Research*, Vol. 23, No. 4, 1999, pp. 733–738.

[11] T. Moyer, *Formulation for Observed and Computed Values of Deep Space Network Date Times for Navigation.* Monograph 2, Deep Space Communications and Navigation Series, 2000.

[12] R. Park, D. Scheeres, G. Giampieri, J. Longuski, and E. Fischbach, "A Test of General Relativity: Estimating the Parameterized Post-Newtonian Parameters from Spacecraft Radiometric Measurements," *Journal of Spacecraft and Rockets*, Vol. 42, No. 3, 2005, pp. 559–568.

[13] G. Bierman, *Factorization Methods for Discrete Sequential Estimation*, Vol. 128. Academic Press, 1977.